Phys. Rev. Applied, in press (2021)

Carrier dynamics and absorption properties of gold-hyperdoped germanium: insight into tailoring defect energetics

Sashini Senali Dissanayake,[1] Naheed Ferdous,[2] Hemi H. Gandhi,[3] David Pastor,[4,3] Tuan T. Tran,[5] Jim Williams,[5] Michael J. Aziz,[3] Eric Mazur,[3] Elif Ertekin,[2] and Meng-Ju Sher[1]

[1)] *Department of Physics, Wesleyan University, Middletown, CT 06459, USA*[a)]

[2)] *Department of Mechanical Science & Engineering, University of Illinois at Urbana-Champaign, IL 61820, USA*

[3)] *John A. Paulson School of Engineering and Applied Sciences, Harvard University, Cambridge, Massachusetts 02138, USA*

[4)] *Departamento de Estructura de la Materia, Física térmica y Electrónica, Facultad de Ciencias Físicas, Universidad Complutense de Madrid, Madrid 28040, Spain*

[5)] *Research school of Physics, Australian National University, Australia*

(Dated: 4 June 2021)

Hyperdoping germanium with gold is a potential method to produce room-temperature short-wavelength-infrared (SWIR; 1.4—3.0 μm) photodetection. We investigate charge carrier dynamics, light absorption, and structural properties of gold-hyperdoped germanium (Ge:Au) fabricated with varying ion implantation and nanosecond pulsed laser melting conditions. Time resolved terahertz spectroscopy (TRTS) measurements show that Ge:Au carrier lifetime is significantly higher than that in previously studied hyperdoped silicon systems. Furthermore, we find that lattice composition, sub-band gap optical absorption, and carrier dynamics depend greatly on hyperdoping conditions. We use density functional theory (DFT) to model dopant distribution, electronic band structure, and optical absorption. These simulations help explain experimentally observed differences in optical and optoelectronic behavior across different samples. DFT modeling reveals that substitutional dopant incorporation has the lowest formation energy and leads to deep energy levels. In contrast, interstitial or dopant-vacancy complex incorporation yields shallower energy levels that do not contribute to sub-band gap light absorption and have a small impact on charge carrier lifetimes. These results suggest that, it is promising to tailor dopant incorporation sites of Ge:Au for SWIR photodetection applications.

I. INTRODUCTION:

Short-wavelength-infrared radiation (SWIR, λ=1.4—3.0 μm) photodetection is important for numerous applications in medicine, industrial imaging, agriculture, telecommunications, and surveillance.[1] Conventional SWIR photodetectors are fabricated from narrow band gap III-V or II-VI semiconductors (e.g., InGaAs, InAs, $Pb_{1-x}Se_x$, $Hg_{1-x}Cd_xTe$) that are heterogeneously integrated with Silicon-CMOS electronics. These approaches result in photodetectors that are expensive, toxic, or require low- temperature to function.[1–3] Development of novel semiconductor materials that overcome these limitations could greatly enhance the applicability of SWIR photodetection. In this study we investigate Ge:Au as a material candidate for Ge-based photodetectors for entire SWIR.

It has recently been shown that Ge:Au is a potential material candidate for low-cost, silicon-compatible room-temperature SWIR photodetection.[4] Ge:Au is Ge supersaturated with high concentrations of Au in a single-crystalline phase. Ge with a band gap energy of 0.67 eV (or 1.66 μm) does not absorb a large fraction of SWIR photons, but the absorption can be red-shifted through Au-dopant-mediated sub-bandgap absorption. Au dopants in Ge produce energy levels that lie near the center of the band gap[5] resulting in a low rate of thermal ionization,[6,7] and hence room temperature SWIR photodetection is possible. Gandhi *et al.* show that Ge:Au exhibits sub-band gap room temperature optoelectronic responses, and the sub-band gap absorption coefficient is comparable to those of commercial SWIR III-V and II-VI materials.[8]

In this work, we fabricate Ge:Au by ion-implantation followed by pulsed laser melting (PLM) and rapid solidification.[9,10] First, Au ions at high concentrations are introduced by ion-implantation. The high dose of dopant ions implanted in Ge results in structural damage and, at high doses, an amorphous surface layer. A single laser pulse is used to melt the defective surface layer. The melt depth extends beyond the damaged layer, and upon cooling, the material resolidifies epitaxially from the substrate into a high-quality single crystal.[9,10] The rapid solidification process must be slow enough to ensure high-quality epitaxial growth and, at the same time, it must be fast enough to trap Au at ultra high concentrations.[11] The properties of hyperdoped-materials depend on the parameters used in ion implantation and laser melting processes.

Previous studies on hyperdoped systems were mainly focused on Si.[12–20] One carrier recombination study in chalcogen-hyperdoped Si reveals lifetimes decrease with increasing dopant concentrations.[18] One ongoing study of Au-hyperdoped Si (Si:Au) shows very short charge carrier lifetimes on the order of 10 ps,[21] but another study reports sub-band gap photodetection out to 2200 nm at room temperature.[10] DFT calculations have previously been applied to Si:Au to investigate the defect formation energy, band structure, and absorption coefficients.[19,20] The DFT results show that the substitutional Au defects in Si are more energetically favorable than the interstitials.[20] Similar to previous Si studies, for hyperdoped Ge, structural and property studies

[a)] Electronic mail: sdissanayake@wesleyan.edu and msher@wesleyan.edu

and theoretical modeling of defect energetics are important for developing sub-band gap optoelectronic devices.

In this work we use a combination of experimental measurements and first principle DFT modeling to characterize and explain the origin of the unique structural and optoelectronic properties of Ge:Au. Specifically, we investigate the charge carrier dynamics, light absorption, and structural properties of Ge:Au fabricated with varying ion implantation and PLM processing conditions. TRTS measurements show that Ge:Au carrier lifetime is significantly higher than that in previously studied hyperdoped silicon systems. We also find that optical and optoelectronic properties of Ge:Au critically depend on the Au lattice position, which can be controlled by specific fabrication conditions.

II. METHODS:

A. Sample fabrication and characterization

In preparing hyperdoped Ge:Au samples, Au ions are implanted at two doses 1×10^{14} or 6×10^{14} cm^{-2} using a 110-keV ion implanter. The samples were tilted 7 degree off the axis normal to avoid channeling and kept at liquid nitrogen temperature during the implants. Heavy ion implantation is commonly known to induce severe morphological change, such as porosity, to Ge substrates. However, keeping the substrate at liquid nitrogen temperature can suppress the porosity up to the dose of 10^{16} cm^{-2}.[22] As a result, the Ge substrate is free of porosity yet amorphized after Au implantation. Following ion implantation, PLM is used to restore the crystallinity. For PLM, a single ns-laser pulse is used to melt the samples at two different laser fluences, 0.24 or 0.49 J/cm^2. The laser wavelength is 355 nm from the 3rd harmonic of a Nd:YAG laser, and the pulse duration is 4-ns FWHM. Previous work showed that the resulting material is single crystalline.[4] The samples are prepared with combinations of the two ion doses and two laser fluences, namely: high dose-high fluence (HD_HF), high dose-low fluence (HD_LF), low dose-high fluence (LD_HF) and low dose-low fluence (LD_LF).

We use TRTS to perform non-contact photoconductivity decay measurements and study carrier recombination dynamics. An amplified Ti:Sapphire femtosecond laser (with 800-nm central wavelength and 2-mJ pulse energy at 1kHz repetition rate) is used for the TRTS experiment. The laser output is split in three by beam splitters where one path generates THz pulses via the air-plasma THz generation method, one path is doubled to 400 nm with a 0.5 mm beta-barium borate (BBO) crystal as an optical pump to excite the charge carriers in the sample, and the last path is used for THz detection using a 1-mm ZnTe electro optical sampling and balanced photodiodes.[23,24] The excited carrier density is 1.9×10^{19} cm^{-3} at which we verified the photoconductivity decay dynamics to be independent of carrier density. After photoexcitation by the pump pulse, the excited charge carriers interact with the THz probe pulse and attenuate the THz signal. The time separation between the pump pulse (duration of 35 fs) and the probe pulse (duration of 1.2 ps) is controlled by a 300-mm delay stage achieving a time window of 2 ns. The time evolution of THz transmission allows us to measure transient photoconductivity decays and evaluate carrier lifetimes with picosecond time resolution.

Rutherford backscattering spectrometry (RBS) is employed to characterize the implanted Au profile, the amorphous layer thickness and the crystal properties of the as-implanted and the post-PLM samples. A monoenergetic 2 MeV He^+ ion beam backscattered from the samples is detected by a solid-state detector at an angle of 100^o. For the as-implanted samples, only the channeling geometry, in which the ion beam is parallel to the [100] axis of the substrates, is employed. This allows us to study the Au distribution and the thickness of the amorphous layer. For the post-PLM samples, both random and channeling geometries are employed for the quantification of the Au redistribution, the crystal quality and, the substitutional/institutional fraction of the implanted species. Analysis of the RBS spectra was done using the SIMNRA simulation program.[25] Considering most scattering events at 2 MeV are single-scattering, the program can use analytical formulae to speed up the simulation. For the electronic stopping power, we chose the SRIM option because it is a semi-empirical database relying on existing experimental data and provides more reliable stopping values.

The optical absorptance (A) of each sample is determined by the measured transmittance (T) and the reflectance (R), and calculated using the relation $A = 1 - T - R$. The transmittance and reflectance of each sample were measured using a UV-VIS-NIR spectrophotometer equipped with an integrating sphere. The optical absorptance of the Ge substrate was also measured for comparison purposes.

B. Computational methods

We simulate Ge:Au using DFT[26,27] employing the Vienna *Ab-initio* Simulation Package (VASP).[28,29] The screened hybrid functional of Heyd, Scuseria, and Ernzerhof (HSE06)[30,31] is implemented for the description of exchange and correlation. This is necessary since standard functionals such as LDA[27] and PBE[32,33] close the band gap in Ge. We used the standard parameters for exchange mixing and range separation with HSE06.

Projector augmented wave (PAW) pseudopotentials are used, and the orbitals are expanded in a plane wave basis set with kinetic energy cutoff of 460 eV. Our optimized lattice constant of bulk Ge, 5.65Å is similar to the experimental value of 5.658Å.[34] The HSE06 obtained indirect (direct) band gap, 0.81 eV (0.90 eV) slightly overestimates the experimental band gap, 0.66 eV[35] (0.80 eV[35]). For defect calculations, 128 atom supercells are used and the Brillouin zone is sampled with a Monkhorst-Pack $2 \times 2 \times 2$ k-point mesh. Total energies are converged within 0.01 eV and atomic coordinates are relaxed until the forces on each atom are less than 0.01 eV/Å.

We consider Au-related defects that are most likely to appear in Ge:Au. Although Au energetically prefers substi-

tutional sites in Ge,[36] both substitutionals Au_{Ge} and tetrahedral interstitials $Au_{i,tetr}$ were considered since the laser-implantation process may result in non-equilibrium defect distributions. Additionally, there is evidence that ion implantation followed by PLM can leave behind a substantial, non-equilibrium population of vacancies that can trap or otherwise interact with the dopant atoms.[19] Therefore, we also consider complexes that may form between Au and vacancies. Amongst the large set of possible interactions, the most common is a single vacancy that traps a diffusing interstitial Au resulting in a divacancy-interstitial Au complex Au_i-2V.[37,38]

For Au_{Ge}, $Au_{i,tetr}$, and Au_i-2V, defect formation energies are obtained by

$$\triangle E_{D,q} = (E_{D,q} - E_{perf}) - \sum_i n_i \mu_i + q(E_v + E_F) \qquad (1)$$

where $E_{D,q}$ is the DFT total energy of the defect incorporating supercell, E_{perf} is the total energy of the supercell with no defect present, n_i is the number of added ($n_i > 0$) or removed ($n_i < 0$) species i (i = Ge, Au) for generating the defect, and μ_i is the atomic chemical potential of the participating species. The chemical potentials μ_{Ge} and μ_{Au} reflect Ge and Au rich experimental conditions, and are obtained by assuming equilibrium with the elemental bulk phases of Ge and Au respectively. The electron chemical potential E_F (Fermi level) is referenced to the DFT valence band maximum E_v.

The optical absorption coefficient α is obtained from the imaginary part of the dielectric function $\varepsilon^{im}(\omega)$ using linear response theory.[39] The real part of the dielectric tensor can then be obtained from the Kramers-Kronig relations.[40] Since the calculated α considers only direct excitations, there may be discrepancies with experimental measurements which also include indirect phonon-assisted transitions.

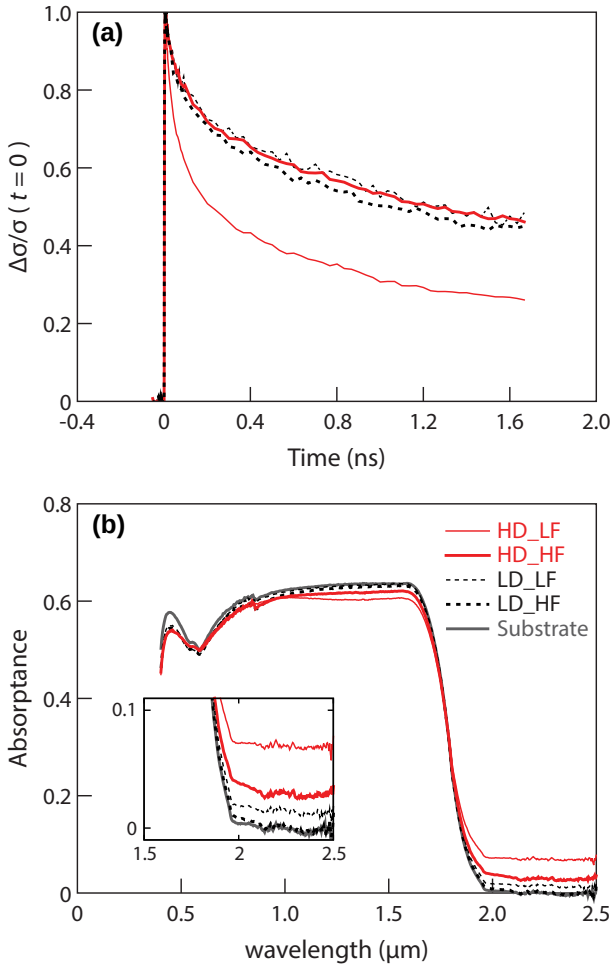

FIG. 1. (a) Photoconductivity of Ge:Au as a function of time. HD_LF (thin red line), HD_HF (thick red line), LD_LF (thin black dashed line) and LD_HF (thick black dashed line) are different samples with different Au doses and PLM fluences. HD_LF has a significantly shorter lifetime than the rest of the samples. (b) Wavelength dependent light absorptance of each sample. The Ge substrate is optically inactive in the sub-band gap region while Ge:Au is optically active and HD_LF has the highest sub-band gap light absorption.

III. STRUCTURAL AND OPTOELECTRONIC PROPERTIES

A. Carrier decay dynamics and structural analysis

Figure 1 (a) shows photoconductivity decay dynamics for the four samples. The half life of photoconductivity decays are 0.86, 1.00, 0.95 and 0.18 ns for LD_HF, LD_LF, HD_HF, and HD_LF, respectively. The HD_HF sample shows similar decay dynamics as the two LD samples, and on the contrary, HD_LF exhibits a significantly shorter lifetime. Figure 1 (b) shows light absorption of each sample with wavelengths ranging from visible to SWIR. Both the substrate and LD_HF has near zero absorptance in the SWIR region. Also in this region, the HD_LF sample shows the highest absorptance compared with the other samples.

The properties of Ge:Au make it more suitable for applications in advanced optoelectronic devices. Ge:Au exhibits long charge carrier lifetimes compared to other hyperdoped materials. Considering Si:Au, a system with demonstrated room-temperature photoresponse to wavelengths as long as 2200 nm, has dopant concentration of 10^{20} atoms/cm^3 and sub-band gap absorption less than 2%.[10] The dopant concentration and sub-band gap light absorption of Si:Au in Ref. 10 are comparable to properties of Ge:Au in this work. Si:Au, however, exhibits charge carrier half-life of 0.005 ns ,[21] while the Ge:Au in this work has half-life two orders magnitude longer. In addition, the lifetime of Si:Au is a strong function of incorporated Au dose,[42] with lifetime decreasing monotonically with increasing Au concentration. On the other hand, carrier lifetime of Ge:Au samples in our study is additionally impacted by different PLM conditions.

Structural differences in Au atom location between these samples are investigated by RBS to shed light on the differences in the charge carrier lifetimes. Figures 2 (a) and (b) show the total and substitutional Au concentrations as func-

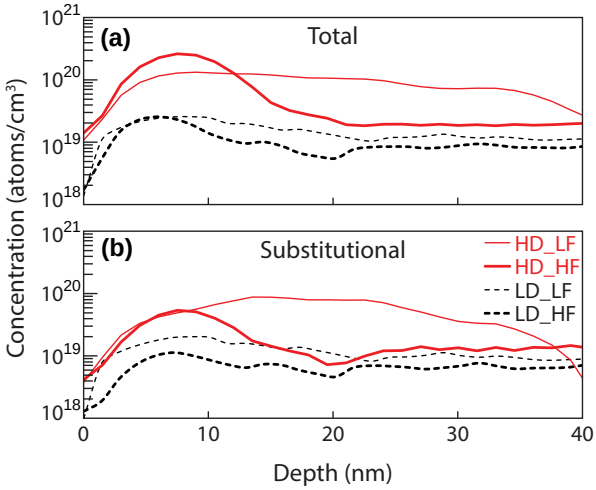

FIG. 2. Structural analysis of Au atom location from RBS measurements. The raw RBS data are shown in Figure S1 in the supplementary material.[41] HD_LF sample has the highest substitutional concentration, and the HD_HF substitutional concentration is similar to LD samples.

tions of depth, respectively. Figure S1 in the supplementary material shows the RBS spectra. The concentration is obtained up to 40 nm, and beyond which the Au spectrum overlaps with the Ge spectrum, limiting our resolution. The structural data, however, is sufficient for us to understand the trends in light absorption and carrier recombination properties. In detail, when performing THz photoconductivity measurements, only the top 14 nm is excited due to the high absorption coefficient of Ge at the optical pump wavelength (400 nm). Comparing the two HD samples, HD_HF is highly segregated towards the surface in both total and substitutional concentration profiles. Considering the substitutional concentration profile, HD_LF has a higher substitutional concentration. Deeper into the sample, HD_HF has concentrations similar to LD samples.

Figure 3 summarizes the experimental results. Figure 3 (a) represents the recombination rate as the inverse of half-life as well as the averaged sub-band gap absorptance from 2.0 to 2.5 μm. Both the recombination rate and the absorptance exhibit similar trends across samples. According to the Shockley-Reed-Hall (SRH) recombination model for defect-assisted carrier trapping and recombination, carrier lifetime should decrease as dopant concentration increases.[43] The SRH model is based on statistics of charge carrier capturing process by deep level trap states which are, in this case, the Au dopants. Assuming a trap state has carrier capture cross section σ and is not filled, the carrier capturing rate is $N_t V_{th} \sigma$, where N_t is the density of the traps and V_{th} is the thermal velocity of electrons. Therefore, the recombination rate would increase with increasing dopant concentration. When the PLM fluence is low (filled triangle symbols), recombination rate indeed increases with Au dose. When the PLM fluence is high (filled circle symbols), on the other hand, the lifetimes of the two samples are comparable and does not exhibit trends predicted by the SRH model. To understand why the recombination rate for HD_HF is slower than expected, we analyze structural properties of the samples in detail.

Figure 3 (b) shows the total and substitutional Au dose by integrating the concentrations depth profile from 0 to 40 nm. The total dose of the two HD samples is approximately one order magnitude higher than the total dose of the two LD samples. Both LD samples are highly substitutional, where the substitutional fraction is 80% and 65% for LF and HF, respectively. The substitutional fraction for HD_LF is 60% and HD_HF is lower at 30%. In the RBS analysis shown in Figures 2 and 3, we find that the amount of substitutional incorporation is strongly dependent on laser fluence. In particular, the HD_HF sample has a significant amount of Au dopant segregated toward the surface, resulting in a lower substitutional incorporation.

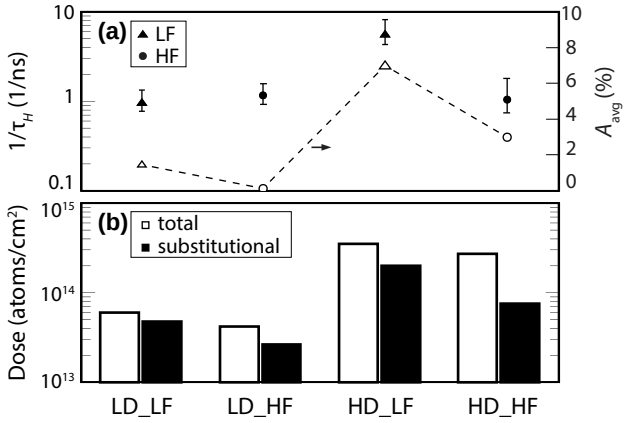

FIG. 3. (a) The inverse of half-lives (filled symbols) and sub-band gap absorptance (unfilled symbols) show similar trends. Triangles and circles represent LF and HF, respectively. (b) Total and substitutional dose of Au in hyperdoped Ge samples from RBS analysis. The unfilled bars and filled bars represent the total and substitutional doses, respectively. HD_LF has the most substitutional Au incorporation, while substitutional Au incorporation in the HD_HF sample is similar to the two LD samples.

Figure 3 (a) shows that the light absorption and carrier recombination rate are both highest in HD_LF, and both properties for HD_HF are similar to the LD samples. Even though the total dose of HD_HF sample is one order magnitude larger than the LD samples, both the recombination rate and the light absorption properties are closer to the LD samples. Comparing the two HD samples, there is a significant difference in substitutional dose. In the HD_HF sample, the majority of the Au dopant resides in sites that are not substitutional, and the non-substitutional dopant has a small impact on charge carrier lifetime or absorption (Supporting Figure S2).[41] To shed light on how the Au atom location site influences properties, we study defect energetics.

B. Defect energetics

Figures 4 (a)–(c) show the three types of defect sites considered in this work, Au_{Ge}, $Au_{i,tetr}$, and a Au_i-2V. Figure 4

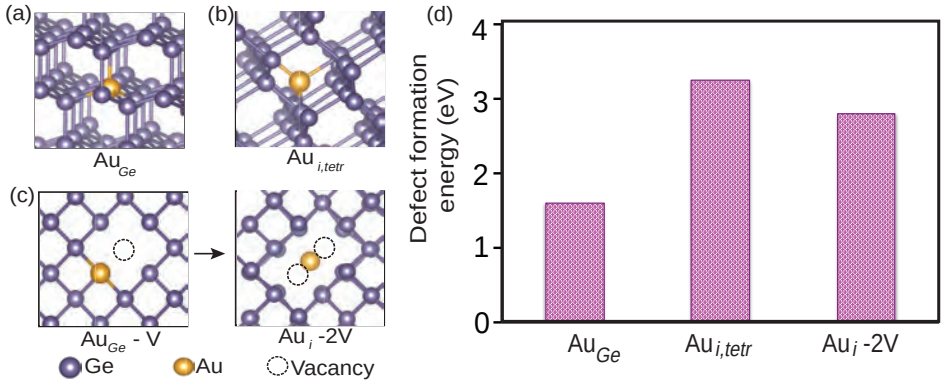

FIG. 4. (a) isolated substitutional, Au_{Ge} (b) tetrahedral interstitial, $Au_{i,tetr}$, (c) gold-vacancy complex, Au_i-2V and (d) the DFT deduced defect formation energies, $E_{D,q}$ of the substitutional Au_{Ge}, interstitial $Au_{i,tetr}$ and impurity-vacancy complex Au_i–2V.

(d) is the calculated formation energies. Formation energies of different defects indicate relative possibility of defect formation. The most possible defect is the one with the smallest formation energy. Due to the ultra-high concentrations, the hyperdoped samples, however, are not in an equilibrium state, and thus other high energy defects can also form. The formation energies are 1.61 eV for Au_{Ge}, 3.25 eV for $Au_{i,tetr}$ and 2.80 eV for Au_i-2V. Au_{Ge} has the lowest $E_{D,q}$ and thus is the most favorable defect in Ge:Au system.

Although Au_{Ge} has the lowest formation energy, the formation of the other defects remains possible. For example, despite its high energy, $Au_{i,tetr}$ may form via kickout or dissociative mechanisms, as believed to occur for Si:Au upon thermal annealing.[44] Also, Au_i-2V can form when a substitutional Au and monovacancy are placed side by side and allowed to relax; the Au atom is attracted towards the vacancy resulting in the lattice distortion as shown in Figure 4 (c). In the final geometry, the Au atom sits in an interstitial site just between two silicon vacancies. Details of the geometries can be found in Ref. 20, where Au_i-2V was shown to play a role in the thermal relaxation of Si:Au. A previous study on Si:Au showed that PLM introduces a high vacancy concentration.[45] If vacancies are also present in hyperdoped Ge, then defect reactions between isolated vacancies and Au_{Ge} can result in Au_i-2V. The binding energy between an Au_{Ge} and a vacancy is determined here to be 1.74 eV.

It is possible to roughly estimate how different defects may impact carrier lifetimes based on their electronic band structure shown in Figure 5. The defect-induced bands are shown in red in all cases. Due to computational resource limitations defects are simulated at a fixed concentration (in 128 atom supercells) of 0.78 % at. Au, a factor of three higher than the experimentally observed HD_LF sample of 0.23% at. This affects the dispersion in the defect levels shown in Figure 5, but it is still possible to capture the main features of the physics from the qualitative nature (Supporting Figure S3).[41] Details of the origin of bands (similar to Au related defects in Si) can be found in Ref. 20.[46]

From Figure 5 (b) we see that Au_{Ge} introduces three (two of which are degenerate) mid gap defect bands. For the 128 atom supercells these bands appear to slightly merge with the valence bands, although this is likely the result of the high simulated concentrations. The Fermi level lies within the defect bands, meaning they are partially filled. Au_{Ge} therefore may serve as a trap for photoexcited electrons in the conduction band or holes in the valence band.

Were it to be present, the isolated defect level of $Au_{i,tetr}$ in Figure 5 (c) would suggest that it may act as a trap, particularly for electrons in the conduction band. These traps are taken as an indication of loss of carrier lifetime.

In Figure 5 (d), the electronic structure of Au_i-2V shows defect levels away from mid-gap, offset towards both the conduction and valence bands. There are no mid-gap defect levels present. We expect that such a defect complex, were it to be present, would have a more benign effect on carrier lifetimes. Although this study provides no direct evidence of Au_i-2V in particular, prior experimental evidence of an Au_i–vacancy complex was found using Au radiotracer diffusion experiments.[47] We note that Au_i-2V is one simple example of a defect complex that may form in Ge:Au, considered here only based on our prior experience with Si:Au. The experimentally realized systems are expected to show a richer phase space of defect complexes. However, this example shows that reduced substitutional fraction may result in complexes, some of which are more benign to transport than the substitutionals defects.

Figure 6 shows the computed absorption spectra for all three defects. Note two main sources of discrepancy between the calculated absorption coefficient and experimentally measured values: the exclusion of indirect phonon-assisted transitions and the large defect concentrations used in the simulations. Our calculated results therefore provide a qualitative understanding.

As Figure 6 shows, the substitutional Au_{Ge} provides the largest sub-band gap absorption, consistent with the partially filled, dispersive mid gap states in the electronic structure. Thus, large incorporation of substitutional Au into our samples would correlate to large optical enhancement. In contrast, $Au_{i,tetr}$ shows the least sub-band gap absorption, due to the presence of only one mid gap defect level. Compared to substitutional Au, the optical response turns on at higher photon energies, since the mid gap level is completely empty

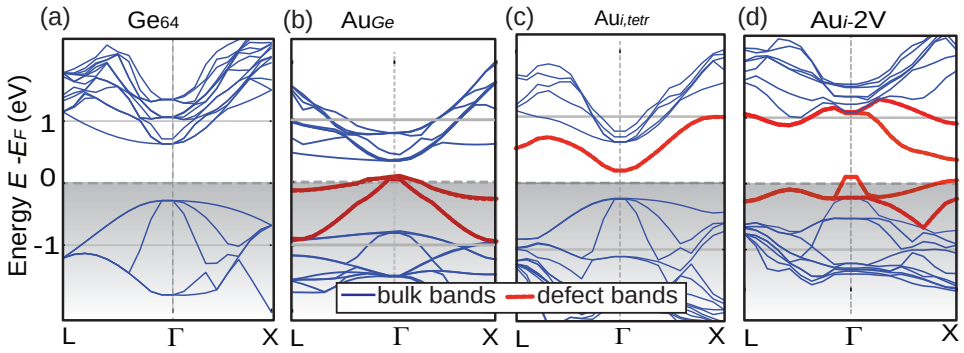

FIG. 5. (a) Band structure of pure Ge, (b) showing localized trap states of Au$_{Ge}$, (c) isolated single energy state from Au$_{i,tetr}$, and (d) delocalized bands coming from Au$_i$-2V. The results are shown for 0.78 % at. concentration of Au. The fermi level is shown by the dashed black horizontal line, below which all bands are filled.

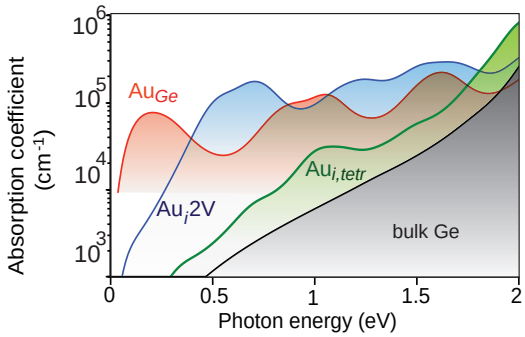

FIG. 6. DFT-HSE06 obtained absorption coefficients of Au$_{Ge}$, Au$_{i,tetr}$, and Au$_i$-2V comparing them with the absorption coefficient of bulk Ge. The HSE06 direct band gap is 0.88 eV.

and allows transitions only from the VB to the defect level itself. Meanwhile, Au$_i$-2V shows sub band gap absorption in between that of Au$_{Ge}$ and Au$_{i,tetr}$, arising from transitions between the defect bands near the VB and the CB. For these more delocalized defect bands, the optical transitions again turn on at higher photon energies than that of Au$_{Ge}$. The boost in absorption below band gap is due to the fact that simulated high concentration causes dispersed defect bands that yield increased defect-defect interaction. The important fact is that the Au$_i$-2V defect bands are not intermediate bands, but are bulk-like bands that will generate absorption near the band edges. For that reason, Au$_i$-2V is not expected to yield sub-band gap absorption and we should focus on the low photon energy region of Figure 6 for qualitative comparison. Note that the HSE06 band gap of Ge is at 0.88 eV, and in Figure 6, the sub-band gap absorption shown for bulk Ge arises as an artifact of the Gaussian smearing used to numerically smooth the behavior. Due to the band gap overestimate in DFT, the precise numerical values where the optical response turns on for each defect may not numerically match the corresponding experimental value. Even so, the trends described with respect to the relative optical activity of the different configurations are expected to hold.

IV. DISCUSSION

Many observed properties of Ge:Au samples can be explained by the DFT simulation results. Most of the samples studied are highly substitutional (above 60% Au substitutional site incorporation), which is consistent with DFT predicting that substitutional Au has the lowest formation energy.

Experimentally we also find correlations between substitutional fraction, lifetime, and absorption strength across samples. First, there is a clear correlation between substitutional dose and sub-bandgap light absorption across samples, where the absorption increases with increasing substitutional dose. Second, the half-life of the samples decreases with increasing substitutional dose. DFT simulations explain these findings by illuminating the different energy levels produced by Au-dopants incorporated on different lattice sites. We find that substitutional Au in Ge produces deep energy levels, whereas interstitial and dopant-vacancy complexes yield shallower energy levels near band edges. Substitutional Au-dopants therefore reduce carrier lifetime and produce strong sub-bandgap light absorption, while non-substitutional dopants have a minimal effect on both carrier lifetime and sub-bandgap light absorption.

This study reveals that controlling defect incorporation site is critical in optimizing Ge:Au optoelectronic properties for SWIR photodetection. The hyperdoping process used is a highly non-equilibrium fabrication method, and PLM fluence affects dopant incorporation. With increasing PLM fluence, the resolidification speed is slower, and less Au dopants are incorporated. Simulations carried out in Ref. 4 show that both melt depth and melt duration increase with fluence. The maximum resolidification velocity decreases at high fluence, leading to less Au trapping (Supporting Figure S4).[41] In our experiment, the HF samples show more segregation in the dopant profiles (Figure 2) with HD_HF mostly segregated toward the surface, whereas the HD_LF sample shows a much more uniform concentration profile. As a result, the HD_HF sample has only 30% of the Au dopants in substitutional sites, lower than the HD_LF sample at 60%, while both the samples have comparable total Au dose. Our results show that

optimizing PLM fluence is crucial for placing Au dopants in substitutional sites.

V. CONCLUSIONS

In summary we carry out experimental and computational analyses to characterize and explain the unique optoelectronic properties of Ge:Au for SWIR photodetection. Ge:Au fabricated using ion-implantation followed by PLM yields high quality materials with high substitutionality for a set of samples with varying Au doses and laser fluences. Sub-band gap absorption is experimentally observed, and the measured charge carrier lifetime is significantly longer than hyperdoped Si. First-principles DFT is employed to find the reason behind high absorption and low carrier lifetime of the HD_LF sample. The formation of isolated intermediate bands for substitutional Au is suggested to give rise to high absorption coefficient while serving as the carrier recombination site. Our study suggests that performance of Ge:Au SWIR photodetectors can be optimized by tailoring the Au implantation and PLM hyperdoping processes to minimize carrier recombination and maximize sub-bandgap absorption.

ACKNOWLEDGMENTS

H.H.G. acknowledges support from the Department of Defense (DoD) under Grant Nos. DGE 0946799 through the National Defense Science and Engineering Graduate Fellowship (NDSEG) Program and the Directed Energy Processing Society Graduate Fellowship. D.P. acknowledges financial support from the MEC within Programa Nacional de movilidad de recursos humanos del Plan Nacional I+D+i 2008-2011 (EX-2010-0662),the program Ramón y Cajal (RYC-2014-16936) and from the Spanish ministry of Science, Innovation and Universities (MICINN) under contract no. TEC2017-84378-R. This work is part of the project MADRID-PV2 P-2018/EMT-4308 funded by the Regional Government of Madrid with support from FEDER funds. This work was also supported by the US Air Force Office of Scientific Research (FA9550-14-1-0150). This work was performed in part at the Harvard Center for Nanoscale Systems (CNS), a member of the National Nanotechnology Infrastructure Network (NNIN), which is supported by the National Science Foundation under NSF award no. ECS-0335765.

DATA AVAILABILITY

The data that support the findings of this study are available from the corresponding author upon reasonable request.

[1] M. P. Hansen and D. S. Malchow, "Overview of SWIR detectors, cameras, and applications," *Thermosense XXX*, **6939**, 94 – 104 (2008).

[2] T. E. Kazior, J. R. LaRoche, D. Lubyshev, J. M. Fastenau, W. K. Liu, M. Urteaga, W. Ha, J. Bergman, M. J. Choe, M. T. Bulsara, E. A. Fitzgerald, D. Smith, D. Clark, R. Thompson, C. Drazek, N. Daval, L. Benaissa, and E. Augendre, "Progress and challenges in the direct monolithic integration of iii–v devices and si cmos on silicon substrates," *2009 IEEE International Conference on Indium Phosphide Related Materials*, , 100–104 (2009).

[3] T. E. Kazior, "Beyond cmos: heterogeneous integration of iii-v devices, rf mems and other dissimilar materials/devices with si cmos to create intelligent microsystems," Philos Trans A Math Phys Eng Sci **372**, 20130105 (2014).

[4] H. H. Gandhi, D. Pastor, T. T. Tran, S. Kalchmair, L. Smilie, J. P. Mailoa, R. Milazzo, E. Napolitani, M. Loncar, J. S. Williams, M. J. Aziz, and E. Mazur, "Gold-hyperdoped germanium with room-temperature sub-band-gap optoelectronic response," Phys. Rev. Applied **14**, 064051 (2020).

[5] L. Johnson and H. Levinstein, "Infrared properties of gold in germanium," Phys. Rev. **117**, 1191–1203 (1960).

[6] E. H. Putley, "Far infra-red photoconductivity," physica status solidi (b) **6**, 571–614 (1964).

[7] N. Sclar, "Properties of doped silicon and germanium infrared detectors," Progress in Quantum Electronics **9**, 149 – 257 (1984).

[8] H. H. Gandhi, *Hyperdoping germanium for SWIR photodetection and high donor activation*, Degree of doctor of philosophy, Harvard university (2019).

[9] J. M. Warrender, "Laser hyperdoping silicon for enhanced infrared optoelectronic properties," Appl. Phys. Rev. **3**, 031104 (2016).

[10] J. P. Mailoa, A. J. Akey, C. B. Simmons, D. Hutchinson, J. Mathews, J. T. Sullivan, D. Recht, M. T. Winkler, J. S. Williams, J. M. Warrender, P. D. Persans, M. J. Aziz, and T. Buonassisi, "Room-temperature sub-band gap optoelectronic response of hyperdoped silicon," Nature Communications **5**, 3011 (2014).

[11] M. J. Aziz, J. Y. Tsao, M. O. Thompson, P. S. Peercy, and C. W. White, "Solute trapping: Comparison of theory with experiment," Phys. Rev. Lett. **56**, 2489–2492 (1986).

[12] T. Gimpel, S. Winter, M. Boßmeyer, and W. Schade, "Quantum efficiency of femtosecond-laser sulfur hyperdoped silicon solar cells after different annealing regimes," Solar Energy Materials and Solar Cells **180**, 168–172 (2018).

[13] F. Liu, M. Wang, Y. Berencén, S. Prucnal, M. Engler, R. Hübner, Y. Yuan, R. Heller, R. Böttger, L. Rebohle, W. Skorupa, M. Helm, and S. Zhou, "On the insulator-to-metal transition in titanium-implanted silicon," Scientific Reports **8** (2018), 10.1038/s41598-018-22503-6.

[14] A. J. Akey, D. Recht, J. S. Williams, M. J. Aziz, and T. Buonassisi, "Single-phase filamentary cellular breakdown via laser-induced solute segregation," Advanced Functional Materials **25**, 4642–4649 (2015).

[15] X. Qiu, Z. Wang, X. Hou, X. Yu, and D. Yang, "Visible-blind short-wavelength infrared photodetector with high responsivity based on hyperdoped silicon," Photon. Res. **7**, 351–358 (2019).

[16] M. Wang, A. Debernardi, Y. Berencén, R. Heller, C. Xu, Y. Yuan, Y. Xie, R. Böttger, L. Rebohle, W. Skorupa, M. Helm, S. Prucnal, and S. Zhou, "Breaking the doping limit in silicon by deep impurities," Phys. Rev. Applied **11**, 054039 (2019).

[17] P. K. Chow, W. Yang, Q. Hudspeth, S. Q. Lim, J. S. Williams, and J. M. Warrender, "Observation of enhanced infrared absorption in silicon supersaturated with gold by pulsed laser melting of nanometer-thick gold films," Journal of Applied Physics **123**, 133101 (2018).

[18] M.-J. Sher, C. B. Simmons, J. J. Krich, A. J. Akey, M. T. Winkler, D. Recht, T. Buonassisi, M. J. Aziz, and A. M. Lindenberg, "Picosecond carrier recombination dynamics in chalcogen-hyperdoped silicon," Applied Physics Letters **105**, 053905 (2014).

[19] W. Yang, N. Ferdous, P. J. Simpson, J. M. Gaudet, Q. Hudspeth, P. K. Chow, J. M. Warrender, A. J. Akey, M. J. Aziz, E. Ertekin, and J. S. Williams, "Evidence for vacancy trapping in au-hyperdoped si following pulsed laser melting," APL Materials **7**, 101124 (2019).

[20] N. Ferdous and E. Ertekin, "Atomic scale origins of sub-band gap optical absorption in gold-hyperdoped silicon," AIP Advances **8**, 055014 (2018).

[21] S. S. Dissanayake, P. K. Chow, J. M. Warrender, and M.-J. Sher, "Improving carrier lifetime of au-hyperdoped si by material tailoring," in *2020 45th International Conference on Infrared, Millimeter, and Terahertz Waves (IRMMW-THz)* (2020) (in press).

[22] T. T. Tran, H. S. Alkhaldi, H. H. Gandhi, D. Pastor, L. Q. Huston, J. Wong-Leung, M. J. Aziz, and J. S. Williams, "Suppression of ion-implantation induced porosity in germanium by a silicon dioxide capping layer," Applied Physics Letters **109**, 082106 (2016).

[23] F. A. Hegmann, O. Ostroverkhova, and D. G. Cooke, "Probing organic semiconductors with terahertz pulses," in *Photophysics of Molecular Materials* (John Wiley Sons, Ltd, 2005) Chap. 7, pp. 367–428.

[24]H. Wen and A. M. Lindenberg, "Coherent terahertz polarization control through manipulation of electron trajectories," Phys. Rev. Lett. **103**, 023902 (2009).
[25]M. Mayer, "Simnra, a simulation program for the analysis of nra, rbs and erda," AIP Conference Proceedings **475**, 541–544 (1999).
[26]P. Hohenberg and W. Kohn, "Inhomogeneous electron gas," Phys. Rev. **136**, B864 (1964).
[27]W. Kohn and L. J. Sham, "Self-consistent equations including exchange and correlation effects," Phys. Rev. **140**, A1133 (1965).
[28]G. Kresse and J. Hafner, "Ab initio molecular dynamics for liquid metals," Phys. Rev. B **47**, 558(R) (1993).
[29]G. Kresse and J. Furthmüller, "Efficient iterative schemes for ab initio total-energy calculations using a plane-wave basis set," Phys. Rev. B **54**, 11169 (1996).
[30]J. Heyd, G. E. Scuseria, and M. Ernzerhof, "Hybrid functionals based on a screened coulomb potential," The Journal of Chemical Physics **118**, 8207–8215 (2003).
[31]A. V. Krukau, O. A. Vydrov, A. F. Izmaylov, and G. E. Scuseria, "Influence of the exchange screening parameter on the performance of screened hybrid functionals," The Journal of Chemical Physics **125**, 224106 (2006).
[32]J. P. Perdew, K. Burke, and M. Ernzerhof, "Generalized gradient approximation made simple," Phys. Rev. Lett. **77**, 3865 (1996).
[33]J. P. Perdew and W. Yue, "Accurate and simple density functional for the electronic exchange energy: Generalized gradient approximation," Physical Rev. B **33**, 8800 (1986).
[34]K. Hummer, J. Harl, and G. Kresse, "Heyd-scuseria-ernzerhof hybrid functional for calculating the lattice dynamics of semiconductors," Physical Review B **80**, 115205 (2009).
[35]K.-H. Kao, A. S. Verhulst, W. G. Vandenberghe, B. Soree, G. Groeseneken, and K. De Meyer, "Direct and indirect band-to-band tunneling in germanium-based tfets," IEEE Transactions on Electron Devices **59**, 292–301 (2011).
[36]A. Almazouzi, J. Bernardini, E. Moya, H. Bracht, N. Stolwijk, and H. Mehrer, "Diffusion, solubility, and thermodynamic properties of gold in solid germanium studied by means of radiotracer and spreading-resistance analysis," Journal of Applied Physics **70**, 1345–1354 (1991).
[37]D. J. Silva, U. Wahl, J. Correia, L. Pereira, L. M. Amorim, M. Da Silva, E. Bosne, and J. Araújo, "Lattice location and thermal stability of implanted nickel in silicon studied by on-line emission channeling," Journal of Applied Physics **115**, 023504 (2014).
[38]S. B. Zhang and J. E. Northrup, "Chemical potential dependence of defect formation energies in gaas: Application to ga self-diffusion," Phys. Rev. Lett. **67**, 2339–2342 (1991).
[39]M. Gajdoš, K. Hummer, G. Kresse, J. Furthmüller, and F. Bechstedt, "Linear optical properties in the projector-augmented wave methodology," Physical Review B **73**, 045112 (2006).
[40]J. S. Toll, "Causality and the dispersion relation: logical foundations," Physical Review **104**, 1760 (1956).
[41]*See Supplemental Material at [URL will be inserted by publisher] for supporting figures for RBS data, further analysis of carrier recombination rate and sub-band gap absorption with substitutional Au dose, defect formation energy change due to change in Au concentration, and simulated maximum recrystallization velocity*.
[42]S. S. Dissanayake, M. Wilkins, P. K. Chow, W. Yang, Q. Hudspeth, S. Q. Lim, J. S. Williams, J. M. Warrender, J. J. Krich, and M.-J. R. Sher, "Figure-of-merit evaluation of gold-hyperdoped silicon for photovoltaic applications," Unpublished.
[43]W. Shockley and W. T. Read, "Statistics of the recombinations of holes and electrons," Phys. Rev. **87**, 835–842 (1952).
[44]W. Yang, Q. Hudspeth, P. Chow, J. Warrender, N. Ferdous, E. Ertekin, G. Malladi, A. Akey, M. Aziz, and J. Williams, "Atomistic mechanisms for the thermal relaxation of au-hyperdoped si," Physical Review Applied **12**, 024015 (2019).
[45]W. Yang, A. Akey, L. Smillie, J. Mailoa, B. Johnson, J. McCallum, D. Macdonald, T. Buonassisi, M. Aziz, and J. Williams, "Au-rich filamentary behavior and associated subband gap optical absorption in hyperdoped si," Physical Review Materials **1**, 074602 (2017).
[46]The defect bands are not formed from Au only. Instead, they are strongly hybridized bands of Au and Ge with mostly Ge in it. The Au *d* level is deep in the valence bands, also hybridized with Ge bulk bands.
[47]M. F. Millea, "The effect of doping on gold diffusion in germanium," Journal of Physics and Chemistry of Solids **27**, 309–314 (1966).

SUPPLEMENTARY MATERIAL

Carrier dynamics and absorption properties of gold-hyperdoped germanium: insight into defect energetics tailoring

Sashini Senali Dissanayake, Naheed Ferdous, Hemi H. Gandhi, David Pastor, Tuan T. Tran, Jim Williams, Michael J. Aziz, Eric Mazur, Elif Ertekin, and Meng-Ju Sher

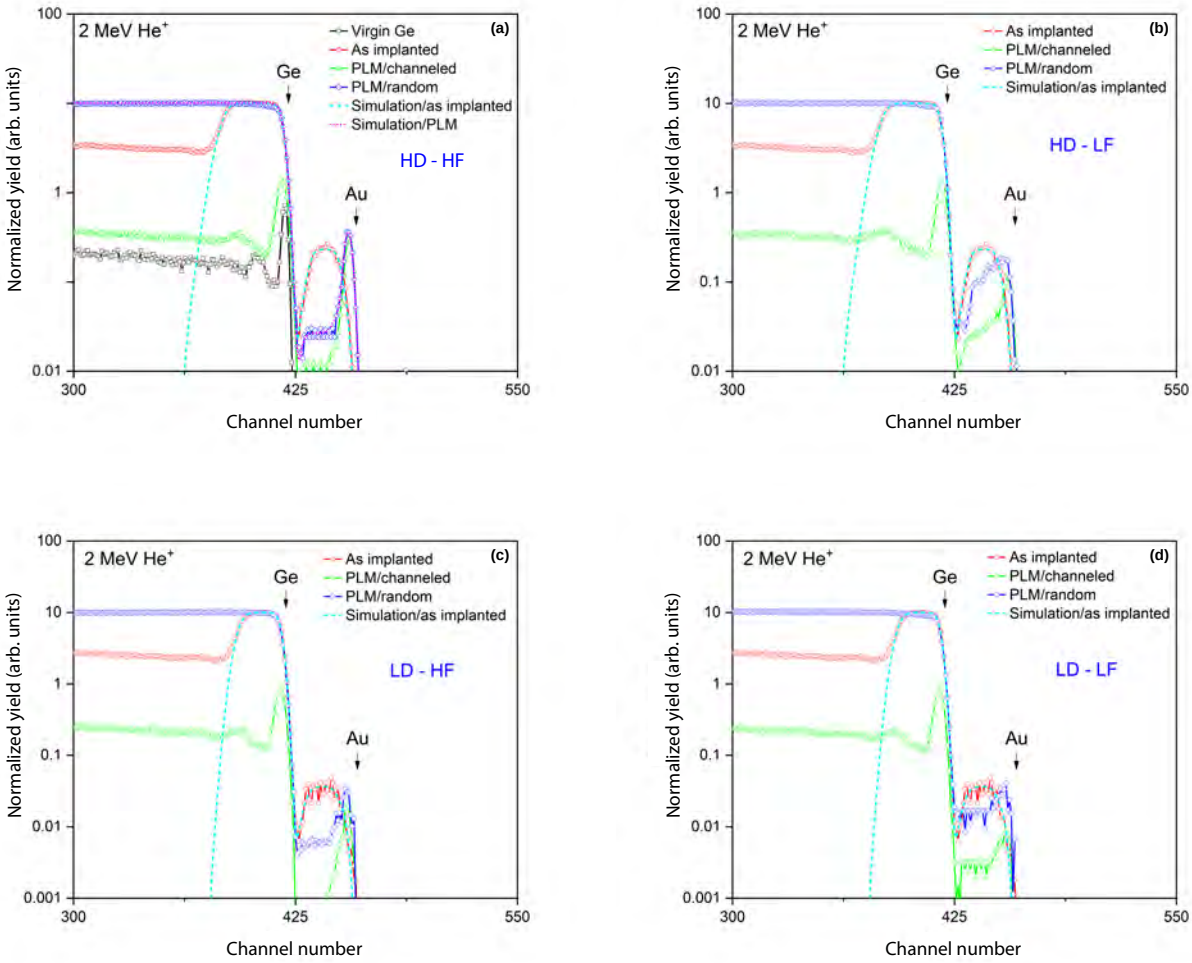

Figure S1: RBS normalized count as a function of the channel number for HD_HF, HD_LF, LD_HF and LD_LF samples in panels (a), (b), (c) and (d) respectively. As-implanted (Red) is the amorphous sample before PLM. PLM/channeled (Green) and PLM/random (Blue) orientations are used to determine the crystallinity and the dopant sites.The virgin Ge substrate is shown by the black curve in panel (a).

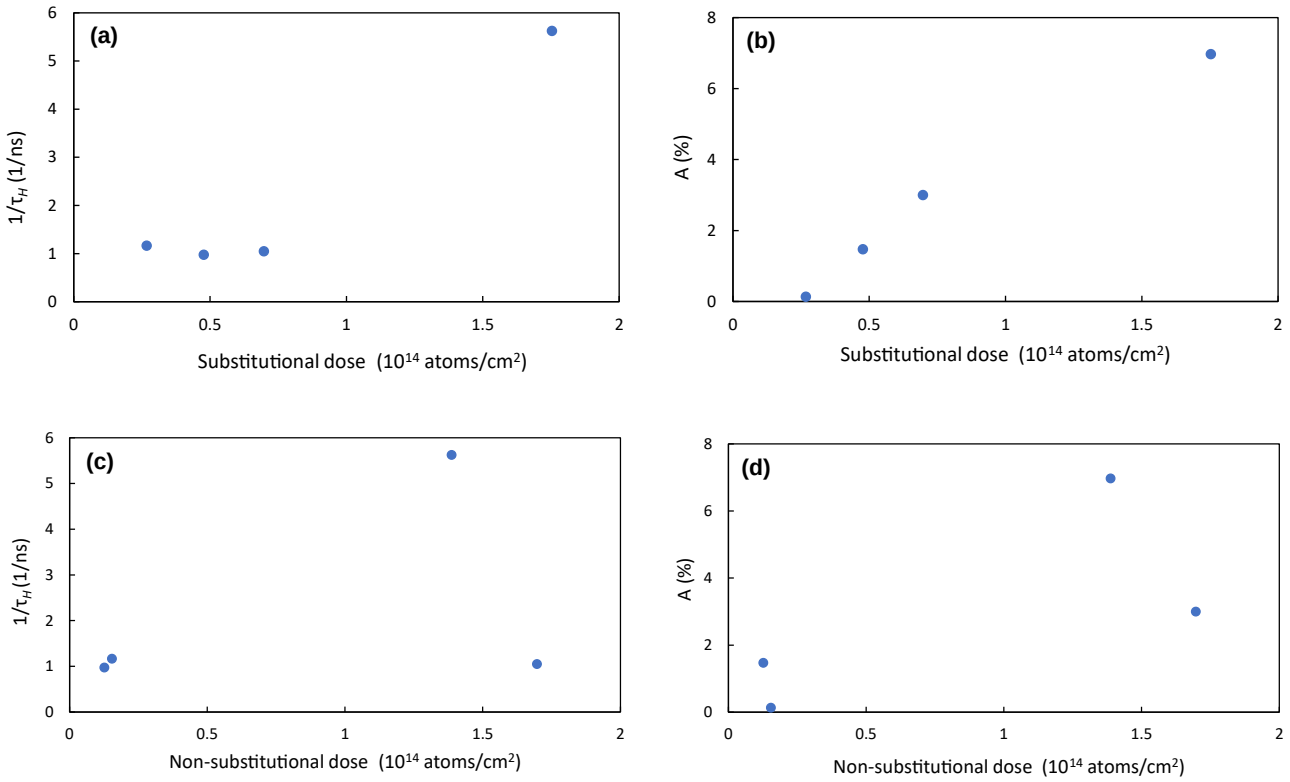

Figure S2: Carrier recombination rate and sub-band gap absorption as a function of substitutional gold dose and non-substitutional gold dose in panels (a), (b), (c) and (d) respectively.

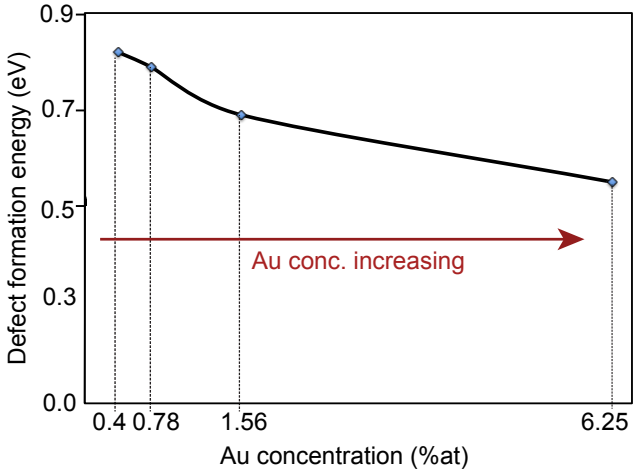

Figure S3: Au_{Ge} defect formation energy change due to change in Au concentration in Ge. This shows that higher Au concentration favors defect formation. Due to limited computational resources, this calculation is done using standard DFT instead of hybrid functional HSE06 shown in the manuscript. Defect formation energy gives the relative probability of different types of defect formation, so that we can infer what defects may most likely form.

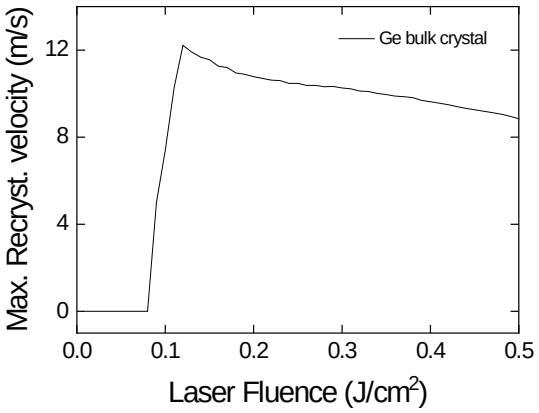

Figure S4: Maximum recrystallization velocity simulated using Laser Induced Melting Predictions (LIMP). The resolidification velocity decreases with increasing laser fluence, and it determines the amount of incorporated Au dopants.